CSMA 2026
17ème Colloque National en Calcul des Structures
18-22 Mai 2026, Presqu'île de Giens (Var)

A Microstructure-Aware OCT–DVC Framework for Full-Field 3D Displacement Measurement in Skeletal Muscle

Iheb Zayani[1,2], Marie Christine Ho Ba Tho[1], Khalil Mansouri[2], Adel Hamdi[2], Olfa Trabelsi[1]

[1] *Université de technologie de Compiègne, CNRS, Biomechanics and Bioengineering, Centre de Recherche Royallieu, CS 60319 - 60203 Compiègne Cedex, France.*
Emails: olfa.trabelsi@utc.fr, marie-christine.ho-ba-tho@utc.fr, iheb.zayani@utc.fr

[2] *École Nationale d'Ingénieurs de Tunis, LR-11-ES19 Laboratoire de Mécanique Appliquée et Ingénierie, Université de Tunis El Manar, 1002 Tunis, Tunisia.*
Emails: adel.hamdi@enit.utm.tn, khalil.mansouri@enit.utm.tn, iheb.zayani@enit.utm.tn

Abstract — In this research paper, a framework that combines OCT imaging and DVC is presented to obtain accurate measurements of full three-dimensional displacement fields inside skeletal muscle at the microscopic scale. Using high-resolution OCT volumes, the method captures the internal deformation of the EDL muscle under incremental load. DVC analysis provides precise, non-invasive quantification of fiber-level kinematics. This technique reveals internal mechanical interactions that are inaccessible with conventional methods.
The proposed combined framework offers a major advance toward non-destructive, experimentally grounded muscle characterization That establishes the foundational first step of a multiscale numerical model for skeletal muscle mechanical behavior.
Keywords — Skeletal muscle, Optical Coherence Tomography, Digital Volume correlation.

1 Introduction

Skeletal muscles possesses a highly hierarchical morphology across different scales. Each structural scale is distinguished by a quasi-periodic/ periodic arrangement of its constituents which gives rise to a scale-specific mechanical properties that defines together the macroscopic (organ-level) mechanical behavior.
Characterizing these properties is key to investigate the muscle function under both physiological and pathological conditions. while the histology is the reference technique to assess muscle morphology, it is an invasive technique that requires excision and fixation of tissue, which changes the microstructure and rules out in vivo applications. Other imaging techniques such as ultrasound [1, 2], magnetic resonance imaging (MRI) [3] and X-ray computed tomography have been extensively applied to muscle imaging [4, 5]. However, these modalities are constrained by the operator dependence and limited field of view of ultrasound, as well as the high cost and long acquisition times associated with MRI. Furthermore, the use of X-ray CT is often restricted by its exposure to ionizing radiation and inferior soft tissue contrast compared to other methods.
Given the limitation of conventional imaging techniques, Optical Coherence Tomography (OCT) arises as an attractive approach to capture skeletal muscle microstructure. Based on the principle of low-coherence interferometry, it offers a non-invasive, high resolution cross-sectional and three-dimensional sample visualisation with real-time acquisition. OCT is commonly applied to study soft tissues such as the cornea [6], the aorta [7] and cartilage [8]. Yet recent works employed OCT in the study of skeletal muscle. For instance, Maillet *et al. 2023* [9] proposed an approach of a non-destructive characterization of the skeletal muscle extracellular matrix morphology by combining OCT with clearing agent and Escobar-Huertas *et al. 2024*[10] employed OCT to study the effect of iodixanol and propylene glycol as clearing agents in extensor digitorum longus and soleus muscles
This paper presents a hybrid experimental and numerical approach to measure a 3D full displacement field in skeletal muscles.In Section 2, we detail the experimental protocol, the image acquisition procedure, and the digital volume correlation framework employed. Section 3 presents the principal results,

and in Section 4, we develop the discussion of these findings and outline the main conclusions.

2 Material and Methods

2.1 Experimental Protocol and image acquisition

In this work, we rely on the experimental data provided by [10]. The experimental protocol employed in the study was conducted in accordance with the ethical regulations outlined by the French veterinary authorities and in accordance with the European Convention for the Protection of Vertebrate Animals Used for Experimental and Other Scientific Purposes (Council of Europe No. 123, Strasbourg 1985).
Three extensor digitorum longus (EDL) muscles were harvested from three 5-month-old Wistar rats and then frozen at -24°C. The animals were maintained in standard cages under controlled conditions of temperature ($21 \pm 1\,^{\circ}$C) and lighting (12:12 hours light/dark). The average weight of the rats was 313 ± 11 g. Rats were sacrificed by isoflurane induction anesthesia followed by pentobarbital sodium injection.
Skeletal muscles presents a hyper-viscoelastic behavior. A stress-relaxation tensile tests were performed using an ElectroForce testBench and planar biaxial machine fitted with a 22 N BOSE load cell, rated at ±1.938 mV/V output to determine the macroscopic mechanical response of the tissue. Muscles were fixed to jaws at the tendon insertion using hooks to remain consistent with the Saint-Venant principle as shown in figure (1). Muscle length was measured 3 times after the thawing with a mean value of 27.30 mm.

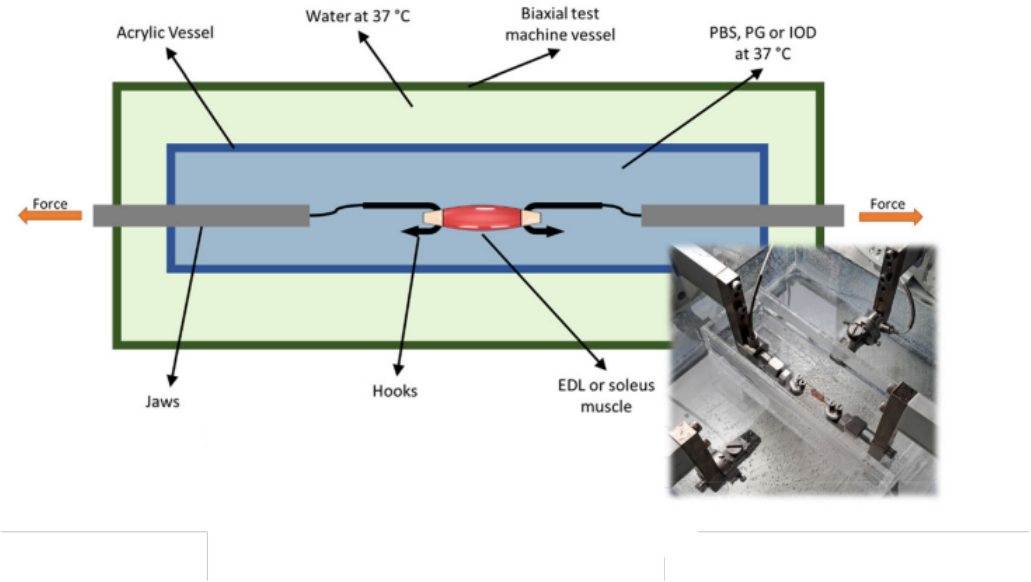

Figure 1: Top view of the experimental setup used for uniaxial tensile testing [10]

A preconditioning deformation of 5% of deformation was applied using 5 triangular signal ramps with a displacement velocity of 0.0005 mm s^{-1} to ensure the redistribution of the internal fluid within the the tissue ECM , minimize the hydrostatic pressure that can alters the stiffness and to guarantee homogeneous results in soft tissues. Subsequently, a step-wise stress-relaxation protocol was implemented, applying 3% deformation increments between consecutive states to achieve strain levels of 8%, 11%, 14% and 17% and a relaxation time of 30 min between increments. The stress–strain response, including the preconditioning phase and the step-wise stress-relaxation loading, is presented in Figure (2).
Image acquisition was performed with Optical coherence tomography (OCT) using a Thorlabs OCT-TEL220C1 system. The system was characterized by a 1300 nm central wavelength, a 36 mm focal length, and a maximum sensitivity of 111 dB at 76 kHz. A field of view of approximately $x = 5$ mm, $y = 2.2$ mm, and $z = 1.5$ mm was chosen to ensure full coverage of the muscle width and to achieve the largest possible measurable volume, with a spatial resolution of $x = y = 5$ μm/pixel and $z = 2.45$ μm/pixel. Images were acquired at the end of each relaxation period for every loading increment to assess muscle microstructure at each stable deformation state, with each image requiring 84 seconds of acquisition.

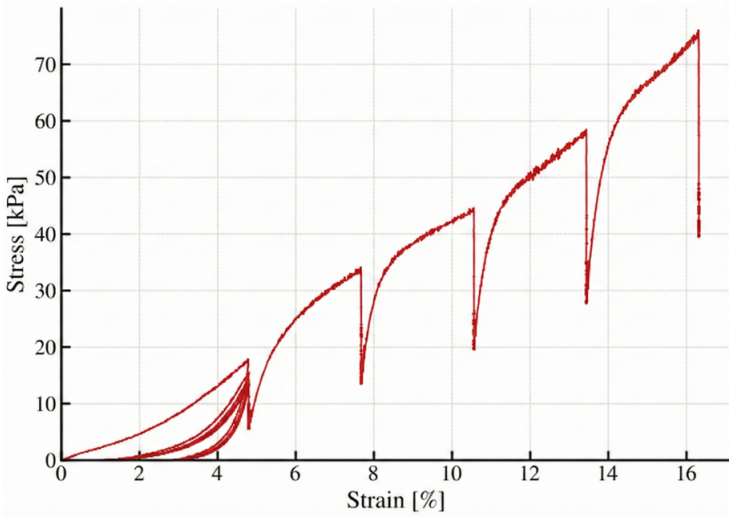

Figure 2: The stress–strain response of the EDL muscle, including both the preconditioning cycles and the subsequent step-wise stress-relaxation loading.

Figure (3) shows a wide-field image of the Extensor Digitorum longus muscle (EDL) with the corresponding OCT scan Field-Of-View (FOV), and figure (4) illustrates two 3D images acquired at 11% and 14% of deformation. These images represent the reference and deformed configurations, respectively, used to compute the displacement fields.

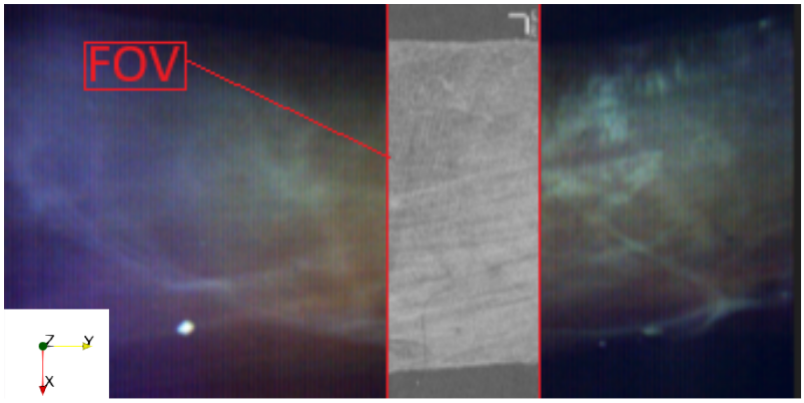

Figure 3: Optical Coherence Tomography (OCT) scanning region on the EDL muscle sample.

2.2 Digital volume correlation

The Digital volume correlation (DVC) was performed using SPAM (The Software for the Practical Analysis of Materials) python package [11]. The software uses a 4x4 matrix called the deformation function Φ (Eq.2) to describe the transformation between two 3D grey-scale images such that :

$$\mathrm{im1}(x) - \mathrm{im2}(\Phi \cdot x) = 0 \tag{1}$$

with

$$\Phi = \begin{bmatrix} F_{zz} & F_{zy} & F_{zx} & t_z \\ F_{zy} & F_{yy} & F_{yx} & t_y \\ F_{zx} & F_{xy} & F_{xx} & t_x \\ 0 & 0 & 0 & 1 \end{bmatrix} \tag{2}$$

The mathematical problem can therefore be posed as finding the mapping Φ that minimizes the square difference between the two images. Thus, the authors define an error functional $\mathcal{T}(\Phi)$, expressed as:

$$\mathcal{T}(\Phi) = \frac{1}{2} \sum_{x \in ROI} \left(\mathrm{im1}(x) - \mathrm{im2}(\Phi \cdot x)\right)^2 \tag{3}$$

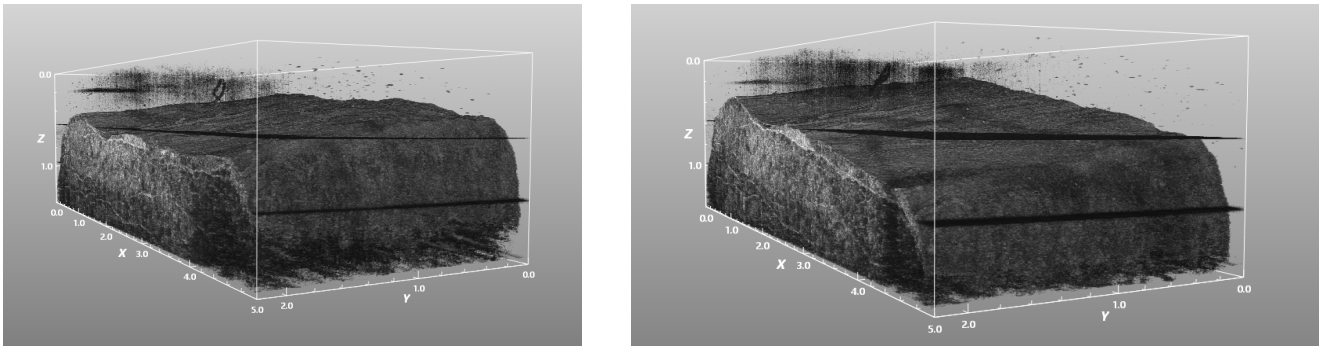

(a) (b)

Figure 4: Three-dimensional OCT images illustrating deformation levels of (a) 11% and (b) 14%.

For a detailed description of the numerical implementation, see [12]. The quasi-periodic heterogeneous microstructure of the EDL muscle results a non homogeneous deformation. To measure the displacement field in the EDL, two SPAM scripts were employed. The first, Spam-pixelSearch, performs a point-by-point pixel search that computes the cross-correlation coefficient of a region of interest (ROI) extracted from the first image using a brute-force search within a specified range in the second image. It measures a displacement field with one-pixel sensitivity that maps the first image onto the second one. Once satisfactory results are obtained, the second script, Spam-ldic, is used. This script takes the output of Spam-pixelSearch as input and performs a local non-rigid correlation on a structured grid; that is, it defines a regular grid of nodes in the first image and runs independent correlations on small subvolumes (correlation windows) centered at each node.

3 Results

This section presents the displacement fields obtained using two SPAM scripts. The displacement fields are computed between a reference image acquired at a global engineering strain of $\varepsilon = 11\%$ and a deformed image acquired at $\varepsilon = 14\%$, as previously mentioned. First, the pixelSearch script compute a global, pixel-sensitive displacement field based on a brute-force cross-correlation. This initial field was then used as the starting estimate for the ldic procedure, which performs local non-rigid correlations on a structured grid to extract a refined, sub-pixel displacement field. Due to the high computational cost for the 3D DVC procedure , a smaller ROI with size of 1000x1000x245 µm (200x200x100 pixels) has been chosen as presented in figure (5). Figure (6) displays the cross-correlation coefficient (CC) distribution

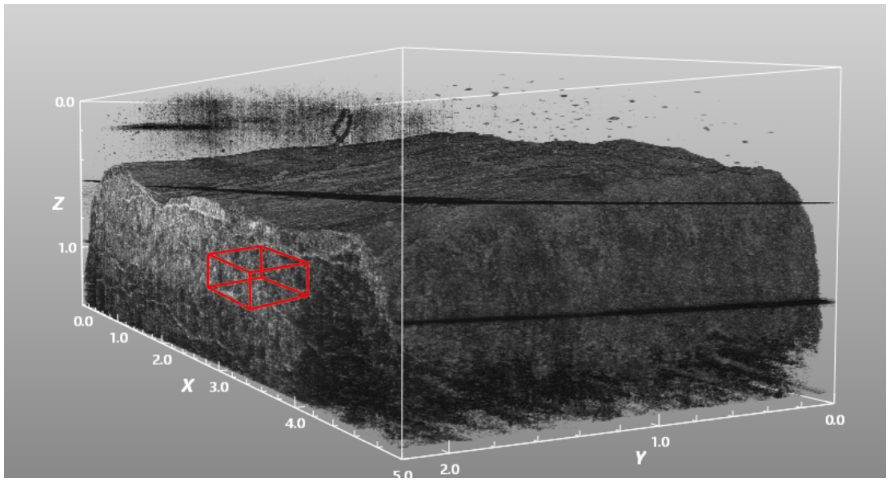

Figure 5: Three-dimensional OCT image and visualization of the Region of Interest (ROI) in the reference configuration, corresponding to a global engineering strain of $\varepsilon = 11\%$.

across the Region of Interest (ROI). The consistently high values (CC > 0.99) indicate a high level of

similarity between the reference and deformed volumes. This validates the displacement field as a reliable initial guess, authorizing the initialization of the sub-pixel convergence step using the Local Digital Volume Correlation script (spam-ldic).

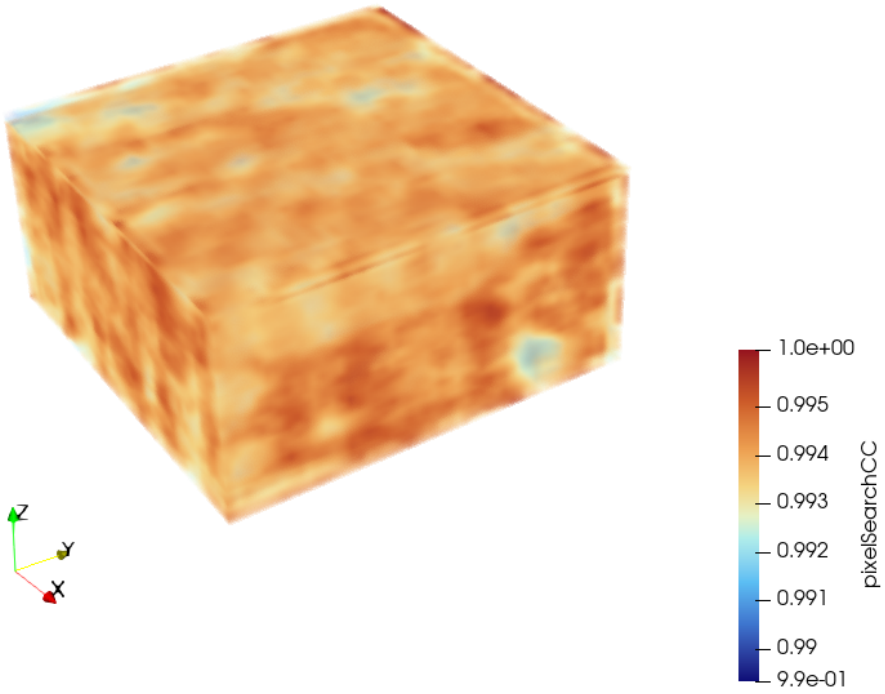

Figure 6: Spatial distribution of the cross-correlation coefficient within the Region of Interest (ROI) at a global engineering strain of $\varepsilon = 14\%$.

The results of the ldic script are reported in Figures (7), (8), and (9). Figure (7) presents the displacement along the loading direction (Y), which corresponds to the fiber direction, together with the corresponding X–Y plane of the OCT 3D image. Figure (8) shows the displacement fields along the transverse (X) and (Z) directions alongside the X–Z plane of the OCT 3D image , all displacement fields in the figures are in μm. Figure (9)shows the results of the spatial distribution of the local convergence indicator.

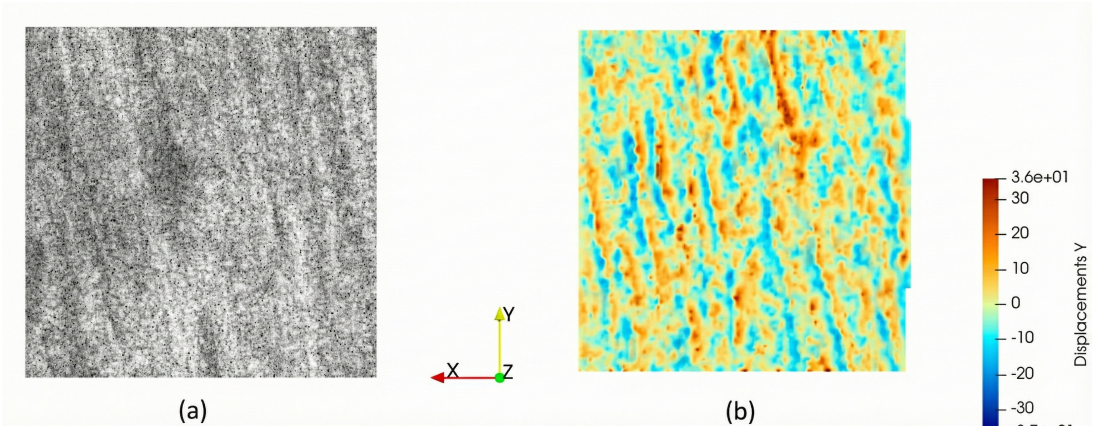

Figure 7: (a) Top view (X–Y plane) of the Region of Interest (ROI) and (b) displacement field along the loading direction (Y-axis), expressed in μm, at a global engineering strain of $\varepsilon = 14\%$.

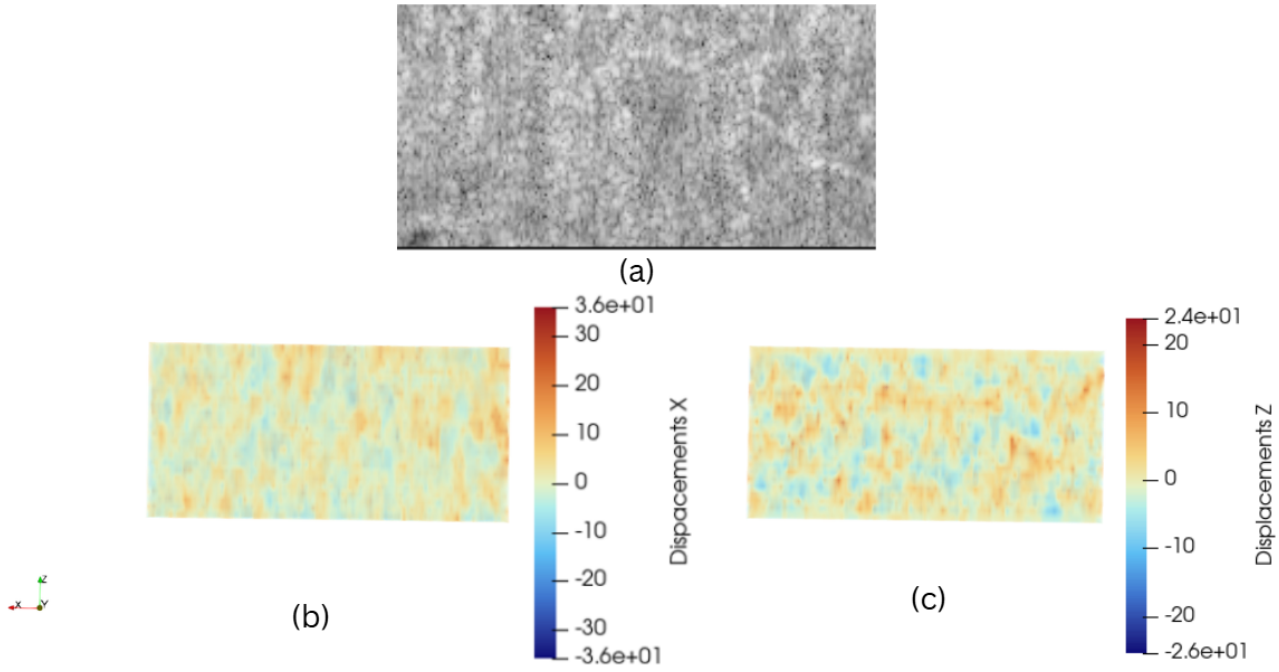

Figure 8: (a) Top view (X–Z plane) of the Region of Interest (ROI), (b) displacement field along the X-axis, and (c) displacement field along the Z-axis, expressed in μm, at a global engineering strain of $\varepsilon = 14\%$.

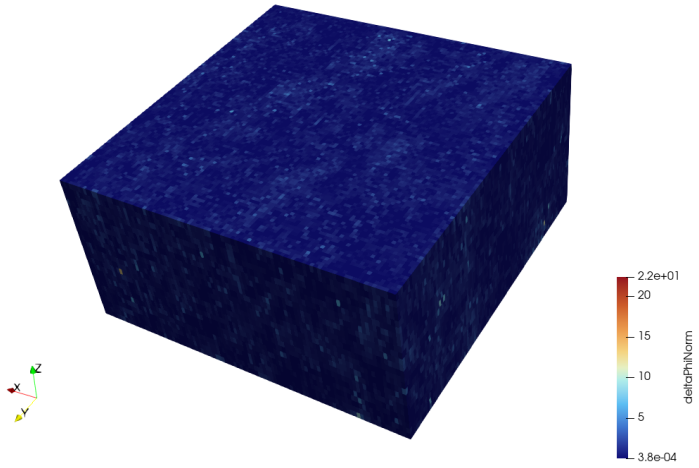

Figure 9: Spatial distribution of the local convergence indicator $\|\Delta\phi\|$ at a global engineering strain of $\varepsilon = 14\%$.

4 Discussion and conclusion

In this section, The spam-pixelSearch results were examined. The results reveals a uniformly high correlation where the cross-correlation values above 0.99 across the entire region of interest (ROI), that highlights good similarity with the OCT volume. Such results reflects the stable acquisition conditions and robust speckle consistency, both are essential primary necessities for accurate DVC analysis. Based on this robust results, the discussion considers the spam-ldic findings which resolve the local micro-scale correlation.

The spam-ldic analysis resolved the 3D displacement fields along all three axes (X, Y, Z). We first examined the SPAM-ldic displacement field along the principal loading direction, corresponding to the axis of

applied force (Y-axis) in the muscle sample. The displacement map along this axis (Figure (7)) exhibits pronounced heterogeneity, reflecting the intrinsic structural organization of the tissue. The digital volume correlation (DVC) analysis revealed anisotropic displacement across the three imaging axes. The maximum displacements observed were largest along the loading direction (Y-axis), with values between 30 and 36 µm. Transverse displacements (X-axis) reached 20–30 µm (Figure (8b)), while on the Z-axis (Figure (8c)), displacements were the smallest, 10–20 µm. These measurements are based on 3D OCT volumes captured near the mid-section of the muscle (Figure (3)), providing the local deformation field within that central region.

The quality of the local digital volume correlation (ldic) was quantified by evaluating an essential measure metric: the convergence behavior (Figure (9). Overall, the results displays that the spam-ldic algorithm accurately tracked the muscle tissue during the tensile test. The results illustrated in Figure (9) highlighted the size of the final adjustment made by the algorithm before it stopped calculating. The dark blue region spans the majority of the ROI indicates that the algorithm found a stable solution. The adjustments became very small (3.8×10^{-4}), meaning the calculation converged smoothly for the muscle tissue. The red and yellow "hotspots" (scattered bright dots) highlight regions where the algorithm struggled to find a match.

In this study, we propose an original methodology that integrates Optical Coherence Tomography (OCT) imaging with Digital Volume Correlation (DVC) to measure the three-dimensional displacement field within the EDL muscle. This methodology allows the visualization of the inner interactions between muscle fibers and the surrounding connective tissue (ECM) at the microscopic scale, offering new insights into the structural mechanics of the muscle. Through the combination of high-resolution data from OCT with experimental displacement measurements from DVC, our approach represents a foundational step toward multiscale modeling of muscle mechanical behavior. This framework lays the groundwork for future studies that aim to link microscale observations to macroscopic mechanical behavior. This leads to a better comprehension of muscle biomechanics and guiding the development of more precise predictive models based on real tissue geometry and experimental data.

References

[1] B. Van Hooren, P. Teratsias, E. F. Hodson-Tole. *Ultrasound imaging to assess skeletal muscle architecture during movements: a systematic review of methods, reliability, and challenges*, Journal of Applied Physiology, American Physiological Society, pp. 978–999, 2020.

[2] M. V. Franchi, B. J. Raiteri, S. Longo, S. Sinha, M. V. Narici, R. Csapo. *Muscle architecture assessment: strengths, shortcomings and new frontiers of in vivo imaging techniques*, Ultrasound in Medicine & Biology, Elsevier, pp. 2492–2504, 2018.

[3] A. M. Heemskerk, B. M. Damon. *Diffusion tensor MRI assessment of skeletal muscle architecture*, Current Medical Imaging Reviews, vol. 3, no. 3, pp. 152–160, 2007.

[4] K. Engelke, O. Museyko, L. Wang, J.-D. Laredo. *Quantitative analysis of skeletal muscle by computed tomography imaging—State of the art*, Journal of Orthopaedic Translation, vol. 15, pp. 91–103, 2018.

[5] L. Borg, J. Sporring, E. B. Dam, V. A. Dahl, T. B. Dyrby, R. Feidenhans, A. B. Dahl, J. Pingel. *Muscle fibre morphology and microarchitecture in cerebral palsy patients obtained by 3D synchrotron X-ray computed tomography*, Computers in Biology and Medicine, Elsevier, pp. 265–269, 2019.

[6] R. M. Werkmeister, S. Sapeta, D. Schmidl, G. Garhöfer, G. Schmidinger, V. Aranha dos Santos, G. C. Aschinger, I. Baumgartner, N. Pircher, F. Schwarzhans, *et al. Ultrahigh-resolution OCT imaging of the human cornea*, Biomedical Optics Express, Optical Society of America, pp. 1221–1239, 2017.

[7] V. A. Acosta Santamaría, M. Flechas García, J. Molimard, S. Avril. *Three-dimensional full-field strain measurements across a whole porcine aorta subjected to tensile loading using optical coherence tomography–digital volume correlation*, Frontiers in Mechanical Engineering, Frontiers Media SA, p. 3, 2018.

[8] S. Nebelung, N. Brill, F. Müller, M. Tingart, T. Pufe, D. Merhof, R. Schmitt, H. Jahr, D. Truhn. *Towards optical coherence tomography-based elastographic evaluation of human cartilage*, Journal of the Mechanical Behavior of Biomedical Materials, Elsevier, pp. 106–119, 2016.

[9] M. Maillet, M. Kammoun, S. Avril, M.-C. Ho Ba Tho, O. Trabelsi, *et al. Non-destructive Characterization of Skeletal Muscle Extracellular Matrix Morphology by Combining Optical Coherence Tomography (OCT) Imaging with Tissue Clearing*, Annals of Biomedical Engineering, Springer, pp. 2323–2336, 2023.

[10] J. F. Escobar-Huertas, J. J. Vaca-González, D. A. Garzón-Alvarado, O. Trabelsi. *Effect of iodixanol and propylene glycol as clearing agents in extensor digitorum longus and soleus muscles: mechanical and morphological characterization using the optical coherence tomography technique*, Biomaterials Science, Royal Society of Chemistry, pp. 5295–5310, 2024.

[11] O. Stamati, E. Andò, E. Roubin, R. Cailletaud, M. Wiebicke, G. Pinzon, C. Couture, R. C. Hurley, R. Caulk, D. Caillerie, *et al. Spam: software for practical analysis of materials*, Journal of Open Source Software, vol. 5, no. 51, p. 2286, 2020.

[12] *SPAM: Software for Practical Analysis of Materials*, spam-project.dev, URL : `https://www.spam-project.dev/docs/tutorials/tutorial-02a-DIC-theory.html`.